



Synergistic photocatalytic-photothermal contribution enhanced by recovered Ag^+ ions on MXene membrane for organic pollutant removal

Qingxiao Zhang^{a,b,1}, Ziping Zhang^{a,1}, Danyang Zhao^a, Lei Wang^a, Hui Li^{a,*}, Fang Zhang^{a,*}, Yuning Huo^{a,*}, Hexing Li^a

^a The Education Ministry Key Lab of Resource Chemistry, Joint International Research Laboratory of Resource Chemistry, Ministry of Education, Shanghai Key Laboratory of Rare Earth Functional Materials, Shanghai Frontiers Science Research Base of Biomimetic Catalysis, and College of Chemistry and Materials Science, Shanghai Frontiers Science Center of Biomimetic Catalysis, Shanghai Normal University, Shanghai 200234, China

^b School of Chemistry and Chemical Engineering, Shandong University of Technology, Zibo 255049, China

ARTICLE INFO

Keywords:

$\text{Ti}_3\text{C}_2\text{T}_x$ MXene
Synergistic photocatalytic-photothermal effect
 Ag^+ ion recovery
Organic pollutant removal

ABSTRACT

The coordinated removal of pollutants in wastewater, especially metal ions and organic pollutants, is regarded as a tough challenge and has focused wide attentions. Synergistic photocatalytic-photothermal route is a powerful technology for the potential wastewater treatment. Herein, we designed a synergistic photocatalytic-photothermal system based on two-dimensional $\text{Ti}_3\text{C}_2\text{T}_x$ MXene (TCM) membrane for simultaneous recovery of Ag^+ ions and removal of aqueous rhodamine B (RhB). The photo-reduction of Ag^+ ions into Ag nanoparticles with the conversion rate up to 100% was achieved on TCM membrane under visible-light irradiation. These Ag nanoparticles uniformly deposited on the surface and interlayers of TCM membrane. It facilitated the separation of photo-generated charges for forming more active species, including both $\bullet\text{O}_2$ and $\bullet\text{OH}$ radicals, to oxidize RhB molecular. At the same time, the surface plasma effect of Ag nanoparticles enhanced the light adsorption and photothermal conversion efficiency ($\sim 81\%$) on the TCM membrane. Conversely, photothermal effect was beneficial for further enhancing the reaction rate of both reduction of Ag^+ ions and photo-oxidation of RhB by concentrating the solution and promoting the electron transfer. The novelty of the synergistic photocatalytic-photothermal contribution is significant for simultaneous recovery of metal ions and removal of organic pollutants in wastewater.

1. Introduction

The large quantities of discharged industrial wastewater impose serious threats on public health and greatly impacts sustainable development of society [1]. The complex contaminants in wastewater, including organics and metal ions, are generally associated with the issues of toxicity, high mobility, non-biodegradability, and easy accumulation in living organisms [2,3]. For the purpose of alleviating the environmental pressure and shortage of water resources, numerous approaches to removing wastewater pollutants have been proposed recently, such as membrane filtration [4], adsorption [5], ozone oxidation [6], electrocatalysis [7], biological routes [8], and *etc.* However, these treatment routes always suffer from low treatment capacity, high energy consumption, and secondary pollutions [9]. Therefore, development of novel methods for the removal of pollutants is necessary

and the utilization of solar energy has garnered increasing interest in recent years, which has been considered very important to meet the long-term global energy demand [10,11]. Among the various utilizations of solar energy, photocatalysis has been considered as an environment-friendly method for removal of pollutants, including organics and metal ions [12–14]. However, its limitations in terms of solar light utilization and low quantum efficiency have not been overcome and have thus raised widespread concerns [15–17]. At the same time, photothermal conversion is an attractive technology for the utilization of solar energy, and has been widely used in water evaporation [18,19], cancer treatment [20], and antimicrobial activities [21,22]. Especially, during the water evaporation process, the solar-to-heat energy conversion achieves high evaporation efficiency *via* the transfer of thermal energy transfer into the surrounding of the system, based on the powerful photothermal materials [23,24]. Although both photocatalytic

* Corresponding authors.

E-mail addresses: lihui@shnu.edu.cn (H. Li), zhangfang@shnu.edu.cn (F. Zhang), huoyuning@shnu.edu.cn (Y. Huo).

¹ Qingxiao Zhang and Ziping Zhang contributed equally to this work.

and photothermal effects have attracted widespread attention, many researchers have studied the combination of photocatalytic and photothermal processes to achieve pollutant removal and clean water simultaneously [4,25]. However, the synergistic photocatalytic-photothermal effect for wastewater treatment, especially the simultaneous recovery of metal ions and degradation of organics, remains to be elucidated.

Unlike the TiO_2 photocatalyst, which is not activated by visible light [26], MXenes, a family of two-dimensional (2D) transition metal carbides and nitrides emerged in recent years, shows the photocatalytic potential by strong absorption of light in a wide range, especially the $\text{Ti}_3\text{C}_2\text{T}_x$ MXene [27–29]. The high surface area and abundant surface functional groups of $\text{Ti}_3\text{C}_2\text{T}_x$ can efficiently facilitate the adsorption of metal ions and organics [30–32]. Meanwhile, MXene shows significant photothermal conversion ability and high thermal conductivity, similar to other carbon-based materials, such as carbon nanotubes and graphene [29]. Therefore, it is significant to study the synergistic photocatalytic and photothermal system based on MXene materials for the removal of organic pollutants, especially assisted with the recovery of metal ions.

Herein, we developed a 2D $\text{Ti}_3\text{C}_2\text{T}_x$ membrane for application in the synergistic photocatalytic and photothermal process for simultaneous recovery of Ag^+ ions and degradation of aqueous rhodamine B (RhB). The photocatalysis reaction rate was improved by the photothermal concentration effect for the solution. Meanwhile, the Ag nanoparticles photo-reduced from Ag^+ ions were uniformly deposited on the $\text{Ti}_3\text{C}_2\text{T}_x$ membrane. It further enhanced the solar-to-heat conversion efficiency owing to the surface plasma effect of Ag nanoparticles, and simultaneously promoted the photocatalytic reaction rate owing to their stronger light absorption and higher migration rate of photo-induced charges. As a result, both recovery of Ag^+ ions and degradation of RhB were greatly improved by means of the synergistic photocatalytic and photothermal contribution. This work provided a novel idea for the treatment of wastewater containing metal ions and organics.

2. Experimental section

2.1. Preparation of $\text{Ti}_3\text{C}_2\text{T}_x$ membrane

$\text{Ti}_3\text{C}_2\text{T}_x$ aqueous dispersions and $\text{Ti}_3\text{C}_2\text{T}_x$ membrane are prepared by improved minimally intensive layer delamination (MILD) method [33–35], as shown in Fig. S1. In a typical process, 10 mL deionized water was added into 30 mL hydrochloric acid (Adamas, 36–38%) in an ice water bath. Then, 3.2 g lithium fluoride (Alfa Aesar, 98%) was dissolved and stirred for 5 min, followed by slowly adding 2.0 g Ti_3AlC_2 powder (Xiyan Materials Co., Ltd., 400 mesh, 99%) within 15 min. It should be pointed out that the etching reaction is carried out in a polytetrafluoroethylene reactor, and the reactor needs to be provided with a vent hole to release the gas generated by the reaction [34,36]. The solution was then stirred at 35 °C for 24 h to selectively etch aluminum in Ti_3AlC_2 . The obtained black solution was centrifuged at 5000 r/min for 5 min, followed with the collection of precipitate. The precipitate was washed twice in 1.0 mol/L hydrochloric acid and five times in deionized water, respectively. In order to achieve the ideal stratification, it was added into 100 mL deionized water to be shaken in turbine oscillator (Multi Reax-Heidolph) for 30 min, and then was sonicated in argon air for 2 h (TitanSonic UC-6, 180 W). The $\text{Ti}_3\text{C}_2\text{T}_x$ aqueous dispersions with the concentration of about 10 mg/mL was finally obtained after being centrifuged for 1 h at 3500 r/min. The concentration of colloidal $\text{Ti}_3\text{C}_2\text{T}_x$ solution was further diluted into 1.0 mg/mL. Then, 10 mL of the solution is filtered at 0.1 MPa for 3 h on a hydrophilic polytetrafluoroethylene (PTFE) membrane (pore size = 0.45 μm , Shanghai Xingya Purification Equipment Co., Ltd.), and dried at 40 °C for 10 h. The obtained $\text{Ti}_3\text{C}_2\text{T}_x$ /PTFE membrane was denoted as TCM.

2.2. Characterizations

X-ray diffraction (XRD) patterns were measured by a D2000 XRD

system (Cu $\text{K}\alpha$, $\lambda = 1.54 \text{ \AA}$, 30 mA, 40 kV). Field emission scanning electron microscopy (FESEM) images and element mapping scans were acquired on a FESEM 4800 with an operating voltage of 3.0 kV. Transmission electron microscopy (TEM) images were obtained on a JEOL-2011 transmission electron microscope. X-ray photoelectron spectroscopy (XPS) was performed on a Perkin Elmer PHI System X-ray photoelectron spectrometer. Inductively coupled plasma spectroscopy (ICP) was tested by VISTA-MPX ICP-OES. UV–vis–NIR absorption liquid spectra were tested by a T6 UV–vis–NIR spectrometer. The optical property was analyzed by UV–vis diffuse reflectance spectra (DRS, UV2450). Electron paramagnetic resonance (EPR) were tested by EPR A300. The temperature detection and thermal image record were conducted on an infrared thermal imaging instrument (FLIR E6390 camera). The shape and size of TCM nanosheets were characterized by Bruker Instruments Dimension Icon using a ScanAsyst-mode atomic force microscope (AFM). The dynamic light scattering analysis was performed by Malvern Zetasizer Nano ZS90. The ζ -potential measurements were recorded on a Zetasizer Nanoseries instrument (Mastersize ZS100). The contact angle of water droplet on the membrane was measured by the sessile drop method at 20 °C on a JC2000D contact angle analyzer. Photocurrent response of different samples was recorded on an electrochemistry workstation (CHI660E) with TCM membrane ($2.0 \times 2.0 \text{ cm}$, 3.5 mg TCM) as work electrode in 50 mL 20 mg/L RhB and 5.5 mg/L AgNO_3 solution, with the potential – 0.3 V vs Ag/AgCl reference electrode and Pt counter electrode. To evaluate the solar-thermal conversion efficiency of the material, infrared thermal imager (FLIR E6390 camera) was used to explore the temperature variation under the irradiation of 808 nm laser (1 W/cm^2). The light to water evaporation efficiency (η_{th}) could be calculated by the following equation (1) [37].

$$\eta_{th} = \frac{m h_{Lv}}{c_{opt} q_i} \quad (1)$$

Where m is the mass flux ($\text{Kg/m}^2\text{h}$), h_{Lv} (KJ/Kg) is the total enthalpy of the liquid-vapor phase change, q_i is the direct solar illumination sun (1.0 kW/m^2), and C_{opt} contributes to the option concentration.

2.3. Activity test

The tests of synergistic photocatalytic-photothermal process were carried out based on the above-obtained TCM membrane. In a typical test, TCM membrane containing 10 mg $\text{Ti}_3\text{C}_2\text{T}_x$ was floated in 30 mL 20 mg/L RhB solution with the stirring rate of 150 r/min. The diameter of the TCM membrane was 3.8 cm and smaller than that of the beaker, which was helpful for the water evaporation. One 300 W xenon lamp (CHF-XM500, light intensity = 3.0 kW/m^2) was located above the TCM membrane with the distance of 15 cm. To make sure that the reaction was really driven by visible-light, all the UV lights with the wavelength less than 420 nm were removed by a glass filter. After reaching adsorption equilibrium within 30 min in the dark, the xenon lamp was turned on. At the same time, the desired amount of AgNO_3 was added in the solution, and the present membrane was denoted as Ag/TCM-X ($X = 1, 3, 5, 7, 9$), where X was the weight ratio (wt%) of Ag^+ ions to 10 mg $\text{Ti}_3\text{C}_2\text{T}_x$. At the given time intervals, the amount of RhB and Ag^+ ions (N) in solution was measured by UV–vis spectrophotometer (T6, Beijing Puxi Instrument Co.) and ICP detection, respectively. It was compared to the initial amount (N_0) to calculate the removal rate. The change of the solution weight was simultaneously recorded for the indicator of water evaporation. The temperature of the reaction system was detected by a FLIR E6390 camera. For comparison, the photocatalytic reaction was conducted as the above process with the cooling system to remain the temperature of solution at 25 °C. Moreover, the thermal effect in the system was explored at the constant temperature of 60 °C. The active species during the reaction process were determined by additionally dissolving 0.050 mmol trapping agents including

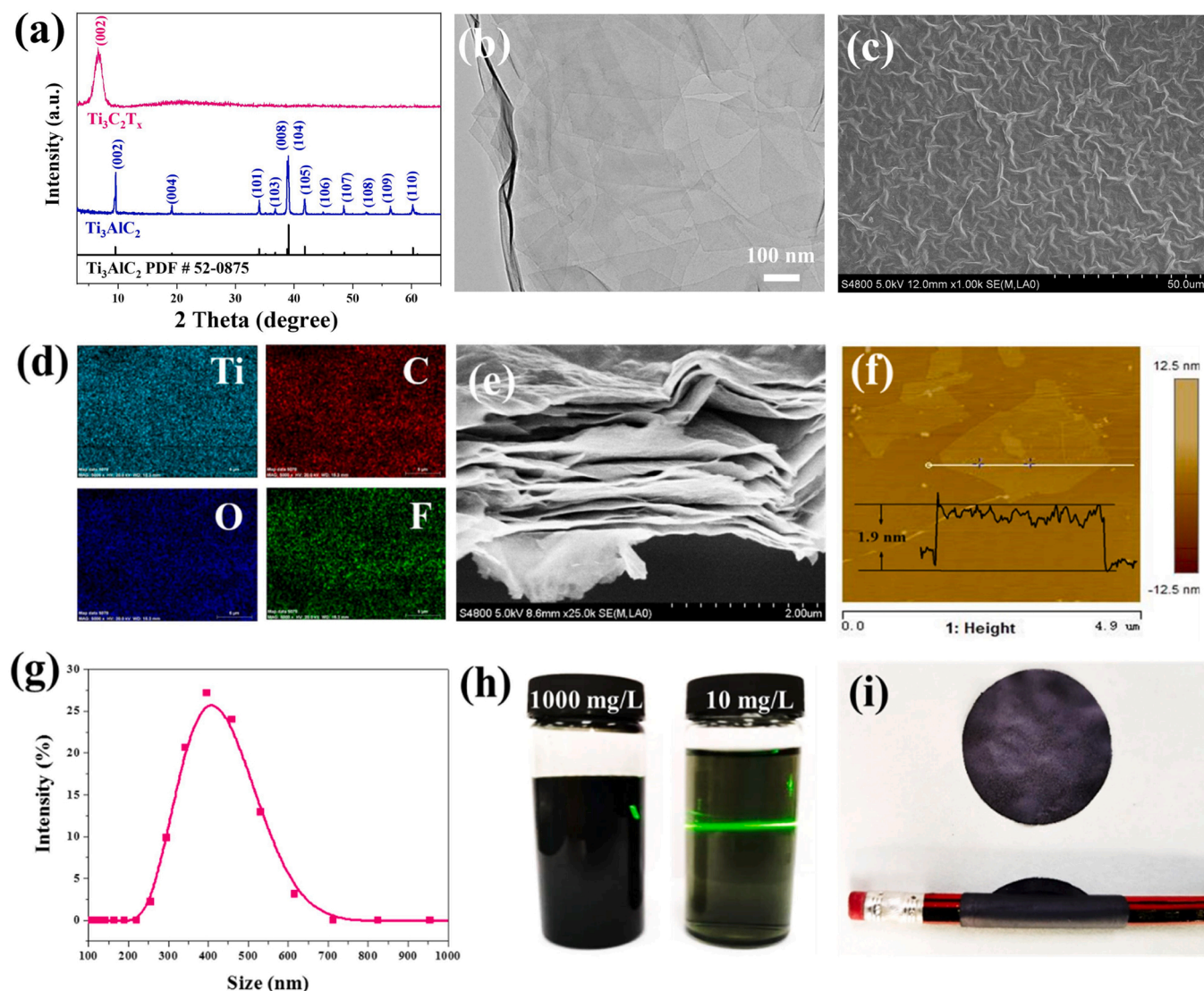


Fig. 1. (a) XRD patterns of Ti₃AlC₂ precursor and TCM membrane without PTFE substrate, (b) TEM image of Ti₃C₂T_x nanosheets, (c) SEM image of the surface of TCM membrane with (d) element mapping images and (e) cross-sectional image, (f) AFM images, (g) dynamic light scattering analysis of Ti₃C₂T_x nanosheets, digital photographs of (h) Ti₃C₂T_x colloidal solution with different concentrations (1000 and 10 mg/L) and (i) TCM membrane without PTFE substrate.

sodium oxalate, K₂Cr₂O₇, tert-butyl alcohol (TBA) and benzoquinone (BQ), which could capture photo-generated holes, photo-generated electrons, ·OH radical and ·O₂ radical, respectively. The reproducibility of the results was checked by repeating the experiments at least three times and was found to be within acceptable limits ($\pm 5\%$).

3. Results and discussion

3.1. Characteristics of TCM membrane

The crystallization of the Ti₃AlC₂ precursor and the obtained TCM membrane without PTFE substrate was initially shown in the XRD patterns (Fig. 1a). The diffraction peaks observed for the commercial Ti₃AlC₂ could be assigned to Ti₃AlC₂ crystal (JCPDS No. 52-0875) [38]. In comparison, the negative shift of (002) peak was obviously present in TCM sample and the other Ti₃AlC₂ peaks disappeared. This indicated the successful exfoliation of the Al layers after the selective etching process and the complete conversion into the MXene material [39–41]. The TEM image (Fig. 1b) showed the graphene-like Ti₃C₂T_x nanosheets with obvious wrinkles at the edges. The planar feature of Ti₃C₂T_x and TCM sample could be further confirmed by the SEM images (Fig. 1c and S2).

Additionally, the corresponding element mapping images of the TCM membrane revealed the uniform distribution of different elements (Fig. 1d). The cross-sectional SEM image of TCM membrane (Fig. 1e) showed a well-aligned multilayer structure, suggesting that the Ti₃C₂T_x nanosheets were self-restacked into a compact structure owing to their inter-sheet interactions during the filtration process. The thickness of the Ti₃C₂T_x nanosheets was determined from the AFM image (Fig. 1f) to be about 1.9 nm, which proved that Ti₃C₂T_x was peeled off as a single layer [39]. Dynamic light scattering analysis was performed on the Ti₃C₂T_x colloidal solution, as shown in Fig. 1g. The average size of the Ti₃C₂T_x nanosheets was about 410 nm. At the same time, the Ti₃C₂T_x colloidal solution at high concentration (1000 mg/L) was non-transparent with a black color (Fig. 1h). In contrast, the Ti₃C₂T_x colloidal solution at low concentration (10 mg/L) presented a transparent and hydrophilic nature with a green color, and showed an obvious Tyndall effect with uniform dispersion [42]. Both of these solutions could be stably existed without agglomeration, due to the electrostatic repulsion between adjacent nanosheets (the ζ -potential of Ti₃C₂T_x colloidal solution was -41.6 mV) [43]. The free-standing nature of the TCM membrane (without PTFE substrate) with the flat surface could be determined by wrapping it on a pencil, as shown in Fig. 1i. It facilitated the separation

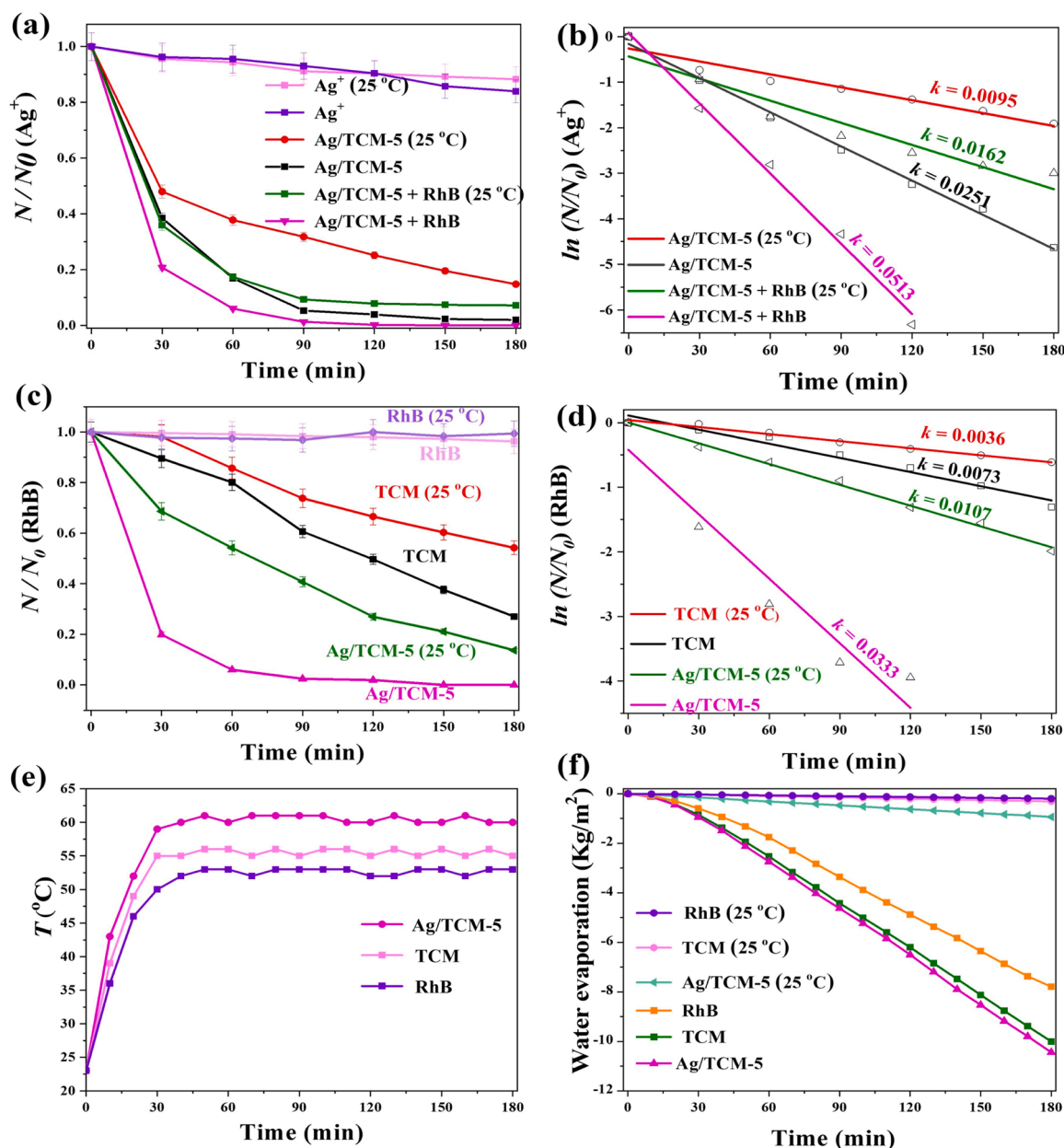


Fig. 2. (a) Evolutions of Ag^+ ion removal on Ag/TCM-5 membrane under different conditions with (b) kinetic curves, (c) evolution of RhB removal with (d) kinetic curves, (e) temperature evolutions, and (f) water evaporation on Ag/TCM-5 and TCM membranes under different conditions. Test conditions: one TCM membrane (10 mg $\text{Ti}_3\text{C}_2\text{T}_x$), 30 mL solution, 26 mg/L AgNO_3 , 20 mg/L RhB, 150 r/min, one 300-W xenon lamp (3.0 kW/m^2 , $\lambda > 420 \text{ nm}$).

and removal of contaminants in practical applications.

3.2. Investigation of synergistic photocatalytic-photothermal contribution

The removal of Ag^+ ions and RhB without using TCM membrane or light irradiations was initially investigated at different temperature, respectively. Fig. S3a-b showed that light irradiation and a high temperature (60 °C) could not induce obvious removal of Ag^+ ions since the high percentage of Ag^+ ions was still existed in the Ag^+ solution. Meanwhile, the addition of RhB was also not helpful for the removal of Ag^+ ions, and the degradation of RhB in dark was invalid in different systems involving TCM membrane and/or Ag^+ ions, at room temperature (25 °C) and higher temperature (60 °C), as shown in Fig. S3c-d.

Although neither the light irradiation nor RhB molecular was not helpful for the removal of Ag^+ ions, it could achieve the high removal percentage of ~80% on TCM after 3 h under visible light irradiation at

the constant temperature of 25 °C, as shown in Fig. 2a. Unfortunately, it was difficult to remove the residual Ag^+ ions, indicating the limitation of TCM for the recovery of Ag^+ ions. However, the rapid removal of Ag^+ ions on TCM membrane could be achieved within 90 min and reached almost 100% without cooling water under visible light irradiation. It was obviously resulted from the effect of synergistic photocatalytic-photothermal contribution. According to Fig. S4a, the content of Ag^+ ions could not influence the crystallization of TCM membrane during the synergistic photocatalytic-photothermal process, since the similar characteristic peaks of MXene could be observed in all Ag/TCM-X samples, beside of other XRD peaks related to PTFE substrate. Meanwhile, the addition of RhB also facilitated the removal speed of Ag^+ ions, especially during the photocatalytic-photothermal process. As shown in Fig. S4b, the increased content of Ag^+ ions enhanced the RhB degradation and Ag/TCM-5 sample presented the highest rate. The excessive Ag^+ ions induced the decreased activity. As a result, kinetic constant (k)

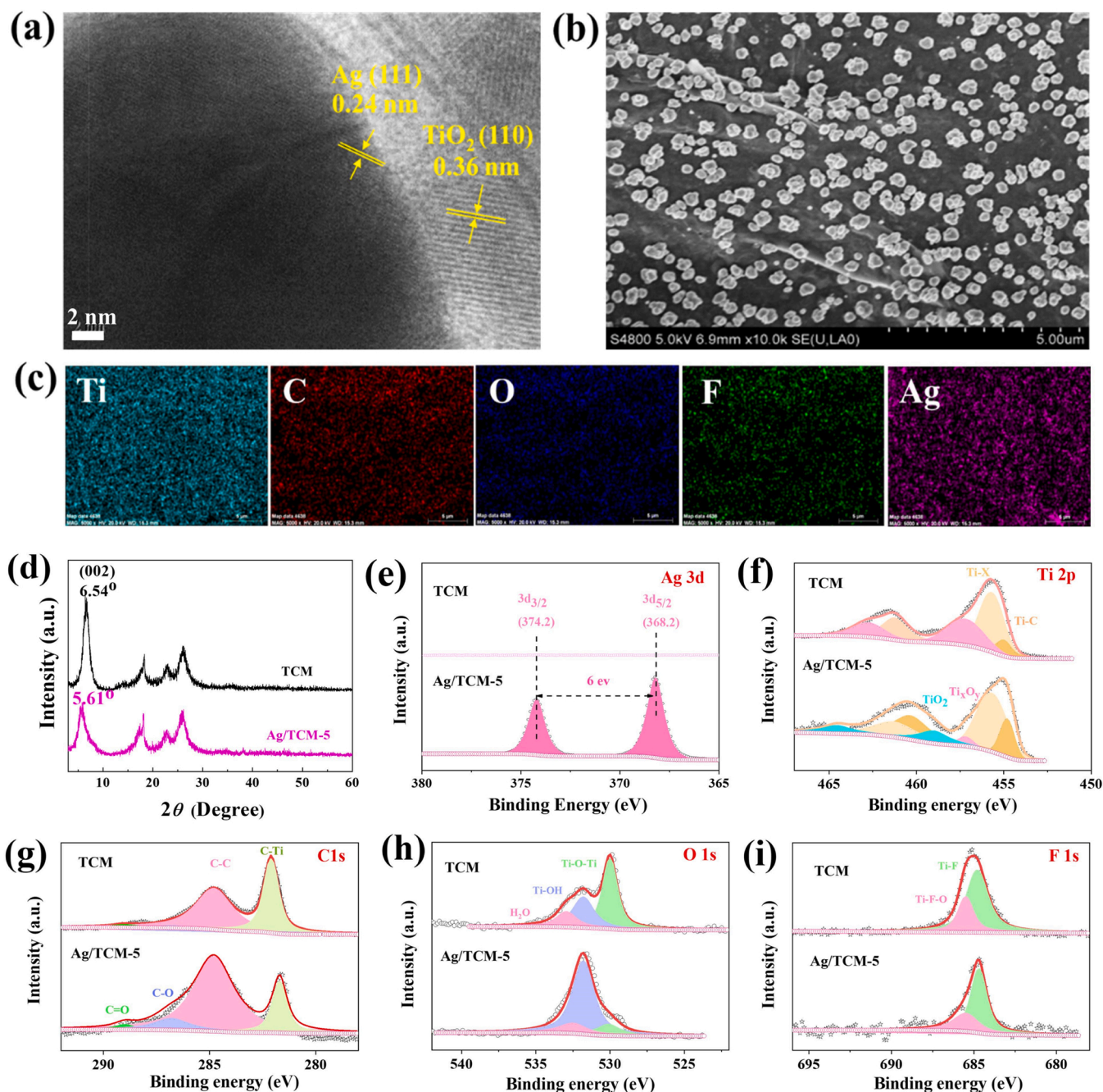


Fig. 3. (a) HRTEM, (b) SEM and (c) element mapping images of Ag/TCM-5, (d) XRD patterns of TCM and Ag/TCM-5; (e) Ag 3d (f) Ti 2p, (g) C 1 s, (h) O 1 s and (i) F 1 s XPS spectrum of TCM and Ag/TCM-5.

of Ag^+ ion removal (0.0251 min^{-1}) via the synergistic photocatalytic-photothermal effect on Ag/TCM-5 sample was higher than that during the photocatalytic process (0.0095 min^{-1}). In addition, the existence of RhB induced the highest k value of Ag^+ ion removal (0.0513 min^{-1}) during the photocatalytic-photothermal process. The degradation of organic RhB in Fig. 2c showed that the photocatalytic-photothermal effect was more powerful than the individual photocatalysis, since the higher RhB degradation rate on Ag/TCM-5 was achieved without cooling water than that at the constant temperature of 25°C . Notably, the addition of Ag ions also significantly improved the RhB photodegradation, especially during the photocatalytic-photothermal process. Therefore, k value of RhB degradation via the synergistic photocatalytic-photothermal effect was higher than that during the photocatalytic process, especially in the existence of Ag^+ ions. k value of

RhB degradation on Ag/TCM-5 sample without cooling water was 0.0333 min^{-1} , which was 9.3-fold higher than that on Ag/TCM-5 at 25°C (0.0036 min^{-1}) and 4.6-fold than that on TCM without cooling water (0.0073 min^{-1}). The increase of k value for both Ag^+ ions removal and RhB degradation on Ag/TCM-5 relative to TCM under different conditions was further compared in Fig. S5, respectively. We could find that the k value of synergistic photocatalytic-photothermal effect was higher than the sum of k values of individual photocatalytic and photothermal effect. It indicated the significance of synergistic photocatalytic-photothermal effect, which was more powerful for the pollutant removal than both photothermal and photocatalytic effect.

At the same time, the significant photothermal conversion led to the promotion of solution temperature up to 55°C on TCM and 60°C on Ag/TCM-5 membrane (Fig. 2e). It ascribed to the excellent light-to-heat

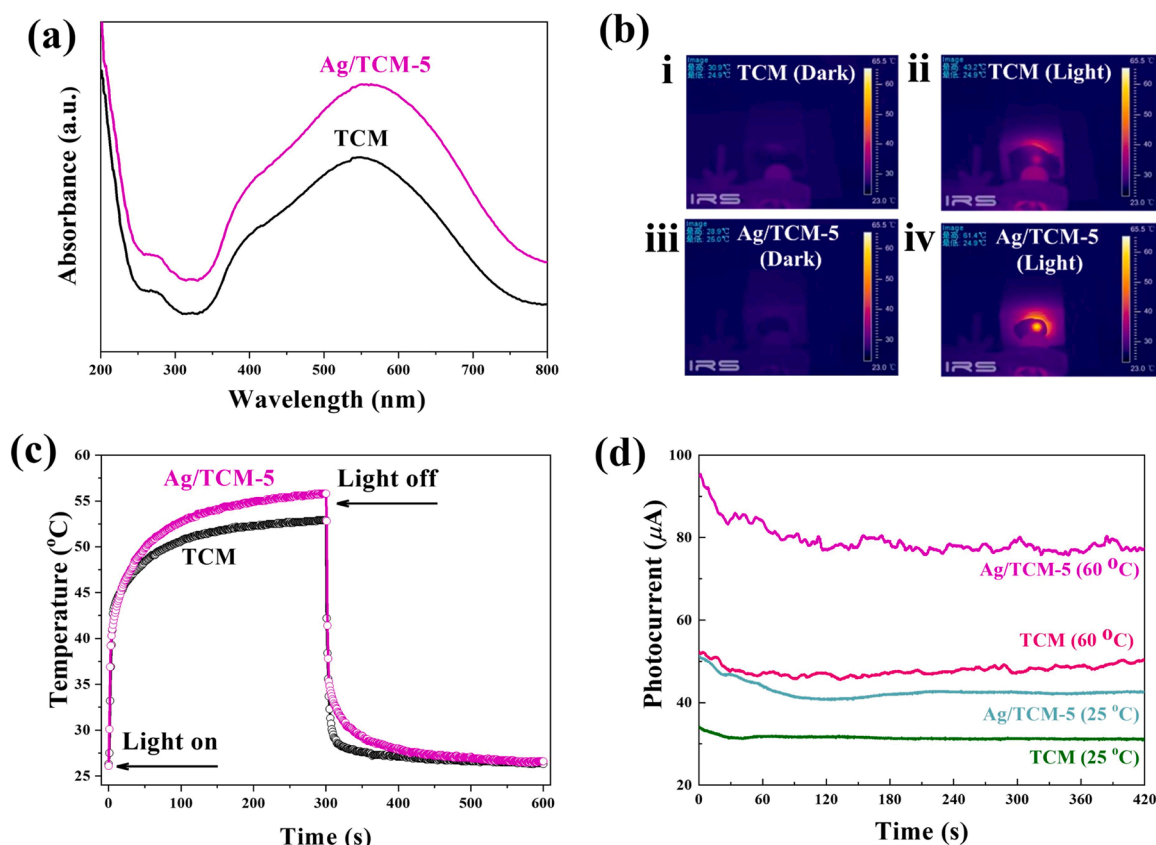


Fig. 4. (a) UV-vis DRS spectra of TCM and Ag/TCM-5. (b) IR thermography images of (i) TCM in dark, (ii) TCM under light irradiation, (iii) Ag/TCM-5 in dark, and (iv) Ag/TCM-5 under light irradiation. Test conditions: 808-nm laser (1 W/cm²), irradiation time = 300 s (c) Temperature evolution profiles of TCM and Ag/TCM-5 recorded on an IR thermal camera under irradiation by 808-nm laser (1 W/cm²). (d) Photocurrent test of TCM and Ag/TCM-5 membranes at 25 and 60 °C. Test conditions: 50 mL solution, 20 mg/L RhB, 5.5 mg/L AgNO₃, work electrode: MXene membrane (2.0 cm × 2.0 cm, 3.5 mg MXene), counter electrode: Pt electrode, 0.2 V vs. Ag/AgCl electrolyte, 300 W Xe lamp (3.0 kW/m², λ > 420 nm), distance = 10 cm.

conversion ability of both MXene and Ag species [29,44], and thus the reaction system can be heated quickly under light irradiation. As a result, the efficient water evaporation on both TCM and Ag/TCM-5 could be achieved, leading to the purified water, as shown in Fig. 2f. The light-to-water-evaporation efficiency of TCM and Ag/TCM-5 were determined to be 77.2% and 81.0%, respectively (see the calculation details in Supporting Information). The efficient water evaporation could induce the concentration of solution and thus facilitate the removal of pollutant. In addition, the content of Ag⁺ ions was not obviously effective to the elevation of solution temperature and the water evaporation (Figs. S6).

After the removal of Ag⁺ ions from the solution, the obtained Ag/TCM-5 sample was analyzed to determine the chemical transition of Ag⁺ ions. From HRTEM in Fig. 3a, it could be found the lattice spacing of 0.24 nm, corresponding to the (111) lattice plane of metallic Ag. It indicated the reduction of Ag⁺ ions into metallic Ag during the synergistic photocatalytic-photothermal process, which was mainly due to the reducing functional groups on Ti₃C₂T_x nanosheets and the photo-induced electrons [4,45]. The interaction of Ag with Ti₃C₂T_x induced partial lattice distortion of Ti₃C₂T_x with a small amount of Ti oxidized to TiO₂ (0.36 nm for (110) lattice plane) [45]. TEM image of Ag/TCM-5 in Fig. S7 clearly confirmed that Ag nanoparticles loaded on the folds of a two-dimensional layer Ti₃C₂T_x, maintaining the main structure of MXene [46]. SEM image of Ag/TCM-5 in Fig. 3b showed that the reduced Ag nanoparticles were uniformly deposited on the surface of the Ti₃C₂T_x nanosheet. The element mapping images (Fig. 3c) show that all of the Ti, C, O, F, and Ag elements were evenly dispersed in Ag/TCM-5 sample, further indicating the uniform distribution of Ag nanoparticles and the tight combination with TCM. Additionally, SEM images in

Fig. S8 showed that the size of Ag nanoparticles gradually increased with the approximate linear trend via the reaction time. The average diameter of Ag nanoparticles was ~236 nm after reaction for 180 min.

Meanwhile, XRD pattern of Ag/TCM-5 showed the characteristic (002) peak of MXene (Fig. 3d), which was similar to that of TCM. It implied that the reduction of Ag⁺ ions on TCM was difficult to influence the crystallization of MXene. However, the negative (002) peak shift of 0.93° from 6.54° in TCM to 5.61° in Ag/TCM-5 could be obviously found. It corresponded to the *d*-spacing increased from 1.32 nm in TCM to 1.55 nm in Ag/TCM-5, and thus suggested that Ag nanoparticles partially entered into the interlayer of Ti₃C₂T_x nanosheets to extend the lamellar spacing of MXene. The chemical surface states of TCM and Ag/TCM-5 were detected in the XPS spectra in Fig. 3e-i. The Ag species in Ag/TCM-5 could be further determined as the zero-valent metallic Ag (Fig. 3e), since the difference of 6.0 eV between its binding energies at 368.2 and 374.2 eV, corresponding to the Ag 3d_{5/2} and Ag 3d_{3/2}, respectively [4]. As shown in Fig. 3f, Ti 2p spectra composed of Ti 2p_{1/2} and Ti 2p_{3/2}, with a difference of 5.54 eV. In Ti 2p_{3/2} spectrum, four peaks could be assigned to Ti-C (454.8 eV), Ti-X (455.7 eV), Ti-O in Ti_xO_y (457.2 eV), and Ti-O in TiO₂ (459 eV), respectively [47,48]. Ti-X was obtained from a combination of nonstoichiometric TiC_x (x < 1) and titanium oxycarbides. Ti_xO_y was assigned as Ti ions with reduced charge state, and TiO₂ was the product of further oxidation of Ti_xO_y. In Ag/TCM-5, the decreased Ti_xO_y content and the increased TiO₂ content after the reduction of Ag⁺ ions into metallic Ag nanoparticles, could be attributed that the reduction of Ag⁺ ions was accompanied by the oxidation of Ti³⁺/Ti²⁺. The C 1s spectra in Fig. 3g presented the C-Ti (282.1 eV), C-C (284.8 eV), C-O (286.8 eV), and C=O (289.0 eV) on the surfaces of TCM and Ag/TCM-5 [47]. The less content of C-O and C=O

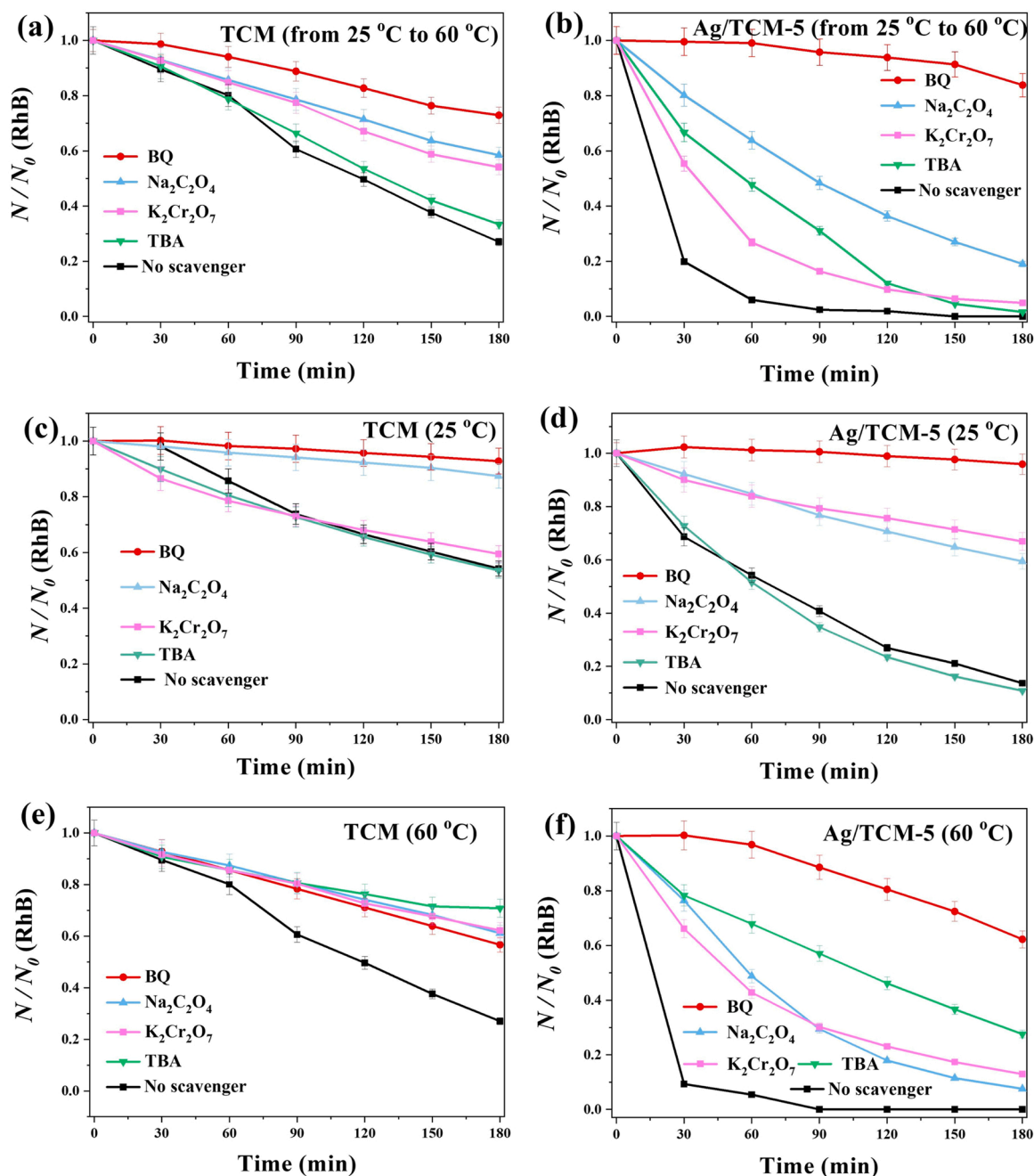


Fig. 5. Trapping tests on TCM and Ag/TCM-5 membranes under different conditions. Reaction conditions: one TCM membrane (10 mg $\text{Ti}_3\text{C}_2\text{T}_x$), 30 mL solution, 20 mg/L RhB, 26 mg/L AgNO_3 , 150 rpm, one 300-W xenon lamp (3.0 kW/m^2 , $\lambda > 420 \text{ nm}$).

groups was possibly related to the oxidation of Ti species. The oxidation process also induced the difference between TCM and Ag/TCM-5 in O 1 s spectra (Fig. 3h). The TCM surface was dominated by Ti-O-Ti vibration (530.2 eV), while the Ag/TCM-5 surface mainly contained Ti-OH vibration (531.8 eV) [49]. The binding state of O also illustrated the oxidation of MXene on the TCM surface. F element was introduced to the MXene surface by the etching process (Fig. 3i), and thus showed both Ti-F at 684.7 eV and Ti-F-O at 686.5 eV [48]. Since F element was not involved in the reduction process, no obvious peak shift could be found in Ag/TCM-5, comparing to that in TCM. Additionally, the distribution of Ag element in Ag/TCM-5 sample during the removal process was investigated by XPS spectra with Ar^+ sputter etching (Fig. S9). Although XPS can only detect at a depth of $\sim 6 \text{ nm}$ in the material [50], XPS signal for Ag/TCM-5 could be obtained to a quite depth by continuous and

undifferentiated Ar^+ sputtering to expose new surface. All the Ag XPS spectra presented the metallic Ag with the difference of 6.0 eV at 368.2 and 374.2 eV. Ag nanoparticles was mainly deposited on the surface of TCM membrane and could be detected at a depth of 500 nm even after reaction of only 5 min. It indicated the rapid reduction of Ag^+ ions on MXene surface. In comparison, metallic Ag nanoparticles almost filled the entire layers of TCM membrane and mainly existed from the surface to the depth of 1000 nm, after reaction of 180 min. It suggested the existence of Ag nanoparticles within the interlayers of TCM membrane, which was consistent with the shift of the (002) peak in the XRD patterns.

The deposition of Ag nanoparticles in the interlayer of TCM membrane greatly influenced its hydrophilic/hydrophobic property. The gradually decreased contact angle could be found in Fig. S10 with the

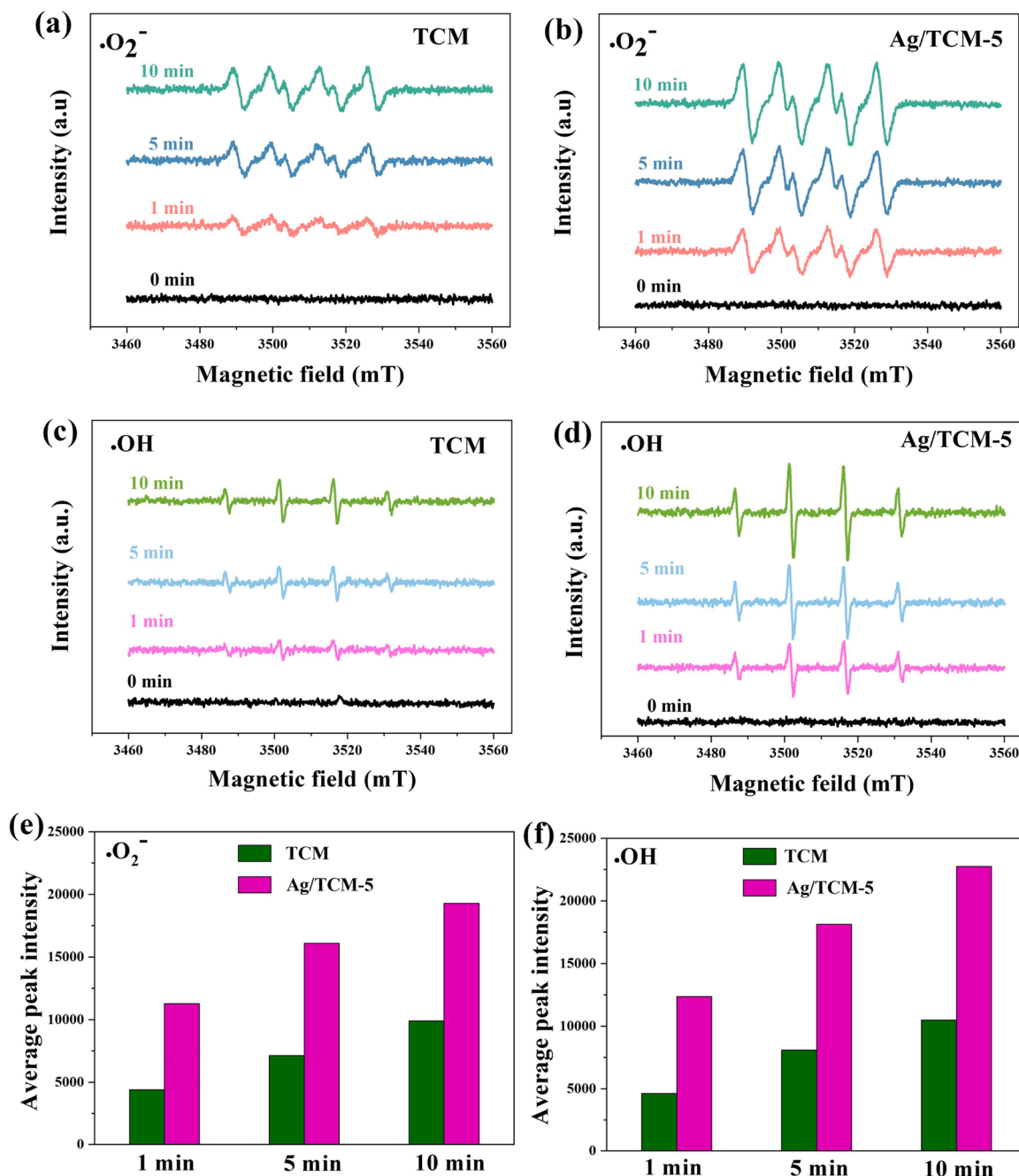
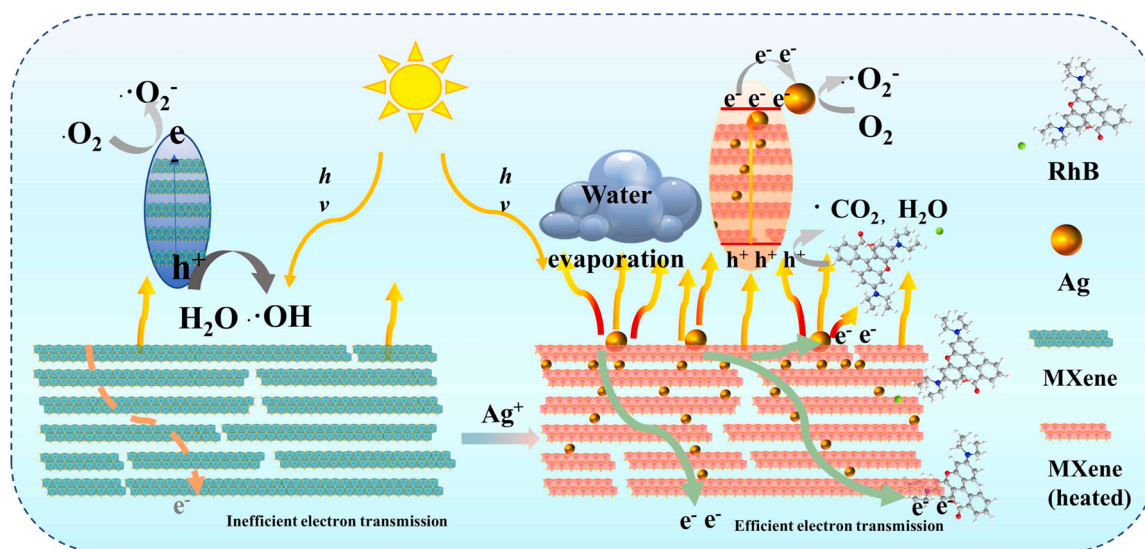


Fig. 6. ESR spectra of $\text{O}_2^{\cdot -}$ radical on (a) TCM and (b) Ag/TCM-5, and $\cdot\text{OH}$ radical on (c) TCM and (d) Ag/TCM-5 under visible light irradiation with 0.05 mmol DMPO scavenger. The average peak intensity of (e) $\text{O}_2^{\cdot -}$ and (f) $\cdot\text{OH}$ on both membranes at different irradiation time. Reaction conditions: one TCM membrane (10 mg $\text{Ti}_3\text{C}_2\text{T}_x$), 30 mL solution, 20 mg/L RhB, 26 mg/L AgNO_3 , 150 rpm, one 300-W xenon lamp (3.0 kW/m^2 , $\lambda > 420 \text{ nm}$).

prolonged reduction time of Ag^+ ions. Therefore, the hydrophobic property of TCM membrane (91.09°) transferred into hydrophilic nature on Ag/TCM-5 sample (69.04°), facilitating the contact with water molecular to improve its evaporation.

UV-vis DRS spectra (Fig. 4a) showed the strong visible-light absorption of TCM in the wavelength region of 400–800 nm, especially within 500–600 nm. The deposition of Ag nanoparticles on TCM further improve the light absorption, due to its surface plasma effect. Additionally, Fig. 4b presented IR thermography images of TCM and Ag/TCM-5 samples under different conditions. Obviously, little thermal effect could be found in dark on both samples. In comparison, the light irradiation of 300 s induced the significant temperature elevation, especially on Ag/TCM-5 sample. Temperature evolution profiles in

Fig. 4c further demonstrated the higher photothermal conversion efficiency of Ag/TCM-5 than that of TCM. It resulted in the high temperature on the surface of Ag/TCM-5 up to 56°C after irradiation for 300 s it was owing to the thermal conductivity (Table S1) and surface plasma effect of Ag nanoparticles in the interlayer of TCM, which obviously facilitated the heat diffusion within the layers [51]. As a result, Ag/TCM-5 significantly increased the photocurrent than TCM at high temperature (60°C), as shown in Fig. 4d, comparing to the smaller photocurrent difference between Ag/TCM-5 and TCM at low temperature (25°C). It was attributed to the enhancement of light absorption and electrical conductivity of Ag nanoparticles (Table S1). Hence, the synergistic removal of Ag^+ ions and RhB with efficient water evaporation, could be ascribed to reduction of Ag^+ ions into Ag nanoparticles by



Scheme 1. Scheme of synergistic photocatalytic-photothermal effect on MXene membrane for the recovery of Ag^+ ions and removal of RhB.

the reductive groups on TCM membrane, and especially photo-induced electrons. It achieved the enhanced light absorption, high photothermal conversion efficiency, and efficient separation of photo-induced charges.

3.3. Synergistic mechanism of Ag^+ recovery and RhB removal

Various active species are responsible for the removal of RhB and Ag^+ ions. In order to determine the main reactive specie during different processes, $\text{Na}_2\text{C}_2\text{O}_4$, $\text{K}_2\text{Cr}_2\text{O}_7$, TBA and BQ were used as the trapping agents for h^+ , e^- , $\cdot\text{OH}$, and $\cdot\text{O}_2^-$, respectively. During the photocatalytic-photothermal process of the RhB removal (from 25°C to 60°C), Fig. 5a-b confirmed that $\cdot\text{O}_2^-$ played the important role on TCM and especially on Ag/TCM-5, since the lowest activity was resulted from the addition of BQ. In contrast, both h^+ and $\cdot\text{O}_2^-$ acted as the main active species on TCM membrane during photocatalytic oxidation (at constant 25°C) (Fig. 5c) and all the active species during photocatalytic oxidation with high temperature of 60°C (Fig. 5e). It was greatly different from that only $\cdot\text{O}_2^-$ radical acted as main active species on Ag/TCM-5 under all the conditions (Figs. 5b, 5d, 5f). It implied the dominant role of Ag nanoparticles for the formation of $\cdot\text{O}_2^-$ radical. In consideration of $\cdot\text{OH}$ radical, it could be proved effective on TCM only during photocatalytic oxidation with high temperature of 60°C . However, $\cdot\text{OH}$ radical could play the role on Ag/TCM-5 at both photocatalytic-photothermal process and photocatalytic oxidation with high temperature. It indicated the promotion effect of both Ag-related photocatalysis and photothermal contribution to the formation of $\cdot\text{OH}$ radical.

In order to further explore the effect of Ag nanoparticles for the formation process of different radicals, ESR spectra was performed on TCM and Ag/TCM-5 samples by using 5,5-dimethyl-1-pyrroline *N*-oxide (DMPO) as a spin trapping agent systems [52]. As shown in Fig. 6a-d, six characteristic peaks demonstrated the production of $\cdot\text{O}_2^-$, and four for that of $\cdot\text{OH}$ radical. Signal intensities of all the peaks gradually increased during the light irradiation for 10 min, indicating the continuous generation process of active species. Fig. 6e-f further summarized the average ESR signal intensities on TCM and Ag/TCM-5. It could be found that Ag/TCM-5 induced the much higher intensity of both $\cdot\text{O}_2^-$ and $\cdot\text{OH}$ radicals than TCM, which was consistent with the result of trapping tests. It was ascribed that the deposition of Ag nanoparticles on TCM facilitated the separation of photo-induced hole-electron pairs and then promoted the formation of $\cdot\text{O}_2^-$ and $\cdot\text{OH}$ radicals to oxidize organic compounds.

Accordingly, the possible reaction mechanism of synergistic

photocatalytic-photothermal contribution for simultaneous Ag^+ recovery and RhB removal on MXene membrane was proposed in Scheme 1. Under visible light irradiation, photo-induced electron transferred onto the conduction band of TCM and then induced the reduction of aqueous Ag^+ ions, besides the effect of the reductive nature of TCM. The recovered Ag nanoparticles were uniformly deposited on the surface and interlayers of MXene nanosheets. Consequently, the strong conductivity of Ag nanoparticles further facilitated the efficient separation of photo-generated charges, and then induced more efficient formation of both $\cdot\text{O}_2^-$ and $\cdot\text{OH}$ radicals to oxidize the organics. At the same time, the Ag nanoparticles greatly enhanced the light absorption and photothermal conversion efficiency of MXene, due to the surface plasma effect. The photothermal effect was beneficial for enhancing the reaction rate of both reduction of Ag^+ ions and photo-oxidation of RhB, via the more efficient charge separation. Meanwhile, the oxidation of RhB also facilitated the reduction of Ag^+ ions. These contributions simultaneously presented the significant promotion effect for the synergistic photocatalytic-photothermal process, leading to the high efficiency of both recovery of metal ions and removal of organic pollutants.

4. Conclusions

TCM membrane was successfully prepared by MILD method on the substrate of PTFE membrane. During the simultaneous removal of Ag^+ ions and RhB from wastewater, the photo-reduction of Ag^+ ions on TCM membrane under visible-light irradiation induced the formation of Ag nanoparticles, which could be uniformly deposited on the surface and interlayers of TCM membrane. As a result, the efficient separation of photo-generated charges was facilitated by its strong conductivity, and thus the formation of both $\cdot\text{O}_2^-$ and $\cdot\text{OH}$ radicals was promoted for the oxidation of RhB. Meanwhile, light adsorption and photothermal conversion efficiency on the membrane TCM were enhanced due to the surface plasma effect of Ag nanoparticles. The photothermal effect was beneficial for further enhancing the reaction rate of both reduction of Ag^+ ions and photo-oxidation of RhB. At the same time, the photocatalytic oxidation of RhB promoted the reduction of Ag^+ ions on the surface of TCM. The synergistic photocatalytic-photothermal contribution to the simultaneous recovery of metal ions and removal of organic pollutants provided a potential approach for the practical wastewater treatment.

CRediT authorship contribution statement

Qingxiao Zhang: Investigation, Methodology, Data curation, Writing – original draft. **Ziping Zhang:** Investigation, Methodology, Data curation. **Danyang Zhao:** Investigation, Data curation, Writing – original draft. **Lei Wang:** Investigation, Data curation. **Hui Li:** Conceptualization, Data curation, Writing – review & editing. **Fang Zhang:** Conceptualization, Data curation, Writing – review & editing. **Yuning Huo:** Conceptualization, Data curation, Writing – review & editing, Project administration. **Hexing Li:** Writing – review & editing, Supervision, Project administration.

Declaration of Competing Interest

The authors declare that they have no known competing financial interests or personal relationships that could have appeared to influence the work reported in this paper.

Data availability

Data will be made available on request.

Acknowledgements

This work is supported by National Key Research and Development Program of China (2020YFA0211004), NSFC (21972093, 21974027, and 22076122), Ministry of Education of China (PCSIRT_IRT_16R49), “111” Innovation and Talent Recruitment Base on Photochemical and Energy Materials (No. D18020), Shanghai Government (18230742500, 20ZR1440700, 22ZR1480200, and 19SG42), and Shanghai Engineering Research Center of Green Energy Chemical Engineering (No. 18DZ2254200).

Appendix A. Supporting information

Supplementary data associated with this article can be found in the online version at [doi:10.1016/j.apcatb.2022.122009](https://doi.org/10.1016/j.apcatb.2022.122009).

References

- X. Zhang, J. Wang, B. Xiao, Y. Pu, Y. Yang, J. Geng, D. Wang, X. Chen, Y. Wei, K. Xiong, Y. Zhu, Resin-based photo-self-Fenton system with intensive mineralization by the synergistic effect of holes and hydroxyl radicals, *Appl. Catal. B* 315 (2022), 121525.
- N.F. Adegboyega, V.K. Sharma, K.M. Siskova, R. Vecerova, M. Kolar, R. Zboril, J. L. Gardea-Torresdey, Enhanced formation of silver nanoparticles in Ag⁺-NOM-iron (II, III) systems and antibacterial activity studies, *Environ. Sci. Technol.* 48 (2014) 3228–3235.
- H. Yin, Y. Kuwahara, K. Mori, H. Yamashita, RuPd alloy nanoparticles supported on plasmonic HxMoO_{3-y} for efficient photocatalytic reduction of p-nitrophenol, *Eur. J. Inorg. Chem.* 2019 (2019) 3745–3752.
- Q. Zou, Z. Zhang, H. Li, W. Pei, M. Ding, Z. Xie, Y. Huo, H. Li, Synergistic removal of organic pollutant and metal ions in photocatalysis-membrane distillation system, *Appl. Catal. B* 264 (2020), 118463.
- K. Wang, L. Yang, H. Li, F. Zhang, Surfactant pyrolysis-guided *in situ* fabrication of primary amine-rich ordered mesoporous phenolic resin displaying efficient heavy metal removal, *ACS Appl. Mater. Interfaces* 11 (2019) 21815–21821.
- B. Rao, T.A. Anderson, A. Redder, W.A. Jackson, Perchlorate formation by ozone oxidation of aqueous chlorine/oxy-chlorine species: role of Cl₂O₂ radicals, *Environ. Sci. Technol.* 44 (2010) 2961–2967.
- P. Cao, X. Quan, K. Zhao, S. Chen, H. Yu, Y. Su, High-efficiency electrocatalysis of molecular oxygen toward hydroxyl radicals enabled by an atomically dispersed iron catalyst, *Environ. Sci. Technol.* 54 (2020) 12662–12672.
- R. Tang, Y. Wang, S. Yuan, W. Wang, Z. Yue, X. Zhan, Z.H. Hu, Organoarsenic feed additives in biological wastewater treatment processes: removal, biotransformation, and associated impacts, *J. Hazard. Mater.* 406 (2021), 124789.
- P. Foladori, M. Vaccari, F. Vitali, Energy audit in small wastewater treatment plants: methodology, energy consumption indicators, and lessons learned, *Water Sci. Technol.* 72 (2015) 1007–1015.
- O. Morton, A new day dawning?: Silicon Valley sunrise, *Nature* 443 (2006) 19–22.
- B.M. van der Ende, L. Aarts, A. Meijerink, Lanthanide ions as spectral converters for solar cells, *Phys. Chem. Chem. Phys.* 11 (2009) 11081–11095.
- W. Pei, J. Zhang, H. Tong, M. Ding, F. Shi, R. Wang, Y. Huo, H. Li, Removal and reutilization of metal ions on ZIF-67/GO membrane via synergistic photocatalytic-photothermal route, *Appl. Catal. B* 282 (2021), 119575.
- Y. Bao, C. Lian, K. Huang, H. Yu, W. Liu, J. Zhang, M. Xing, Generating high-valent iron-oxo identical =Fe^(IV)=O complexes in neutral microenvironments through peroxymonosulfate activation by Zn-Fe layered double hydroxides, *Angew. Chem. Int. Ed.* (2022), e202209542.
- Y. Zhou, L. Zhou, Y. Zhou, M. Xing, J. Zhang, Z-scheme photo-Fenton system for efficiency synchronous oxidation of organic contaminants and reduction of metal ions, *Appl. Catal. B* 279 (2020), 119365.
- F. Fu, Q. Wang, Removal of heavy metal ions from wastewaters: a review, *J. Environ. Manag.* 92 (2011) 407–418.
- Xa Dong, W. Zhang, Y. Sun, J. Li, W. Cen, Z. Cui, H. Huang, F. Dong, Visible-light-induced charge transfer pathway and photocatalysis mechanism on Bi semimetal@defective BiOBr hierarchical microspheres, *J. Catal.* 357 (2018) 41–50.
- H. Yin, Z. Chen, Y. Peng, S. Xiong, Y. Li, H. Yamashita, J. Li, Dual active centers bridged by oxygen vacancies of ruthenium single-atom hybrids supported on molybdenum oxide for photocatalytic ammonia synthesis, *Angew. Chem. Int. Ed.* 61 (2022), e202114242.
- H. Huang, L. Zhao, Q. Yu, P. Lin, J. Xu, X. Yin, S. Chen, H. Wang, L. Wang, Flexible and highly efficient bilayer photothermal paper for water desalination and purification: self-floating, rapid water transport, and localized heat, *ACS Appl. Mater. Interfaces* 12 (2020) 11204–11213.
- S. Meng, X. Zhao, C.-Y. Tang, P. Yu, R.-Y. Bao, Z.-Y. Liu, M.-B. Yang, W. Yang, A bridge-arched and layer-structured hollow melamine foam/reduced graphene oxide composite with an enlarged evaporation area and superior thermal insulation for high-performance solar steam generation, *J. Mater. Chem. A* 8 (2020) 2701–2711.
- H. Lin, S. Gao, C. Dai, Y. Chen, J. Shi, H. Lin, S. Gao, A two-dimensional biodegradable niobium carbide (MXene) for photothermal tumor eradication in NIR-I and NIR-II biowindows, *J. Am. Chem. Soc.* 139 (2017) 16235–16247.
- J. Song, H. Liu, M. Lei, H. Tan, Z. Chen, A. Antoshin, G.F. Payne, X. Qu, C. Liu, Redox-channeling polydopamine-ferrocene (PDA-Fc) coating to confer context-dependent and photothermal antimicrobial activities, *ACS Appl. Mater. Interfaces* 12 (2020) 8915–8928.
- G. Yang, H. Yin, W. Liu, Y. Yang, Q. Zou, L. Luo, H. Li, Y. Huo, H. Li, Synergistic Ag/TiO₂-N photocatalytic system and its enhanced antibacterial activity towards *Acinetobacter baumannii*, *Appl. Catal. B* 224 (2018) 175–182.
- B. Lu, F. Qian, Z. Sun, F. Jia, L. Zhang, Photothermal reverse-water-gas-shift over Au/CeO₂ with high yield and selectivity in CO₂ conversion, *Catal. Commun.* 129 (2019), 105724.
- Y. You, F. Cao, Y. Zhao, Q. Deng, Y. Sang, Y. Li, K. Dong, J. Ren, X. Qu, Near-infrared light dual-promoted heterogeneous copper nanocatalyst for highly efficient bioorthogonal chemistry *in vivo*, *ACS Nano* 14 (2020) 4178–4187.
- C. Song, D. Qi, Y. Han, Y. Xu, H. Xu, S. You, W. Wang, C. Wang, Y. Wei, J. Ma, Volatile-organic-compound-intercepting solar distillation enabled by a photothermal/photocatalytic nanofibrous membrane with dual-scale pores, *Environ. Sci. Technol.* 54 (2020) 9025–9033.
- X. Chen, L. Liu, P.Y. Yu, S.S. Mao, Increasing solar absorption for photocatalysis with black hydrogenated titanium dioxide nanocrystals, *Science* 331 (2011) 746–750.
- D. Hu, X. Huang, S. Li, P. Jiang, Flexible and durable cellulose/MXene nanocomposite paper for efficient electromagnetic interference shielding, *Compos. Sci. Technol.* 188 (2020), 107995.
- J. Ran, F.-T. Li, T.-Y. Ma, S.-Z. Qiao, G. Gao, A. Du, F.-T. Li, Ti₃C₂ MXene co-catalyst on metal sulfide photo-absorbers for enhanced visible-light photocatalytic hydrogen production, *Nat. Commun.* 8 (2017) 13907.
- R. Li, L. Zhang, L. Shi, P. Wang, MXene Ti₃C₂: an effective 2D light-to-heat conversion material, *ACS Nano* 11 (2017) 3752–3759.
- Y.-J. Zhang, Z.-J. Zhou, J.-H. Lan, C.-C. Ge, Z.-F. Chai, P. Zhang, W.-Q. Shi, Theoretical insights into the uranyl adsorption behavior on vanadium carbide MXene, *Appl. Surf. Sci.* 426 (2017) 572–578.
- O. Mashtalir, K.M. Cook, V.N. Mochalin, M. Crowe, M.W. Barsoum, Y. Gogotsi, Dye adsorption and decomposition on two-dimensional titanium carbide in aqueous media, *J. Mater. Chem. A* 2 (2014) 14334–14338.
- J. Guo, Q. Peng, H. Fu, G. Zou, Q. Zhang, Heavy-Metal adsorption behavior of two-dimensional alkalization-intercalated MXene by first-principles calculations, *J. Phys. Chem. C* 119 (2015) 20923–20930.
- F. Shahzad, M. Alhabeb, C.B. Hatter, B. Anasori, S.M. Hong, C.M. Koo, Y. Gogotsi, Electromagnetic interference shielding with 2D transition metal carbides (MXenes), *Science* 353 (2016) 1137–1140.
- Y. Zhao, Q. Yu, W.W. Cheng, J.Q. Li, A.Q. Zhang, X. Lei, Y. Yang, S.Y. Qin, Ti₃C₂T_x MXene liquid crystal: access to create background-free and easy-made alignment medium, *ACS Nano* 16 (2022) 5454–5462.
- Q. Yu, C. Su, S. Bi, Y. Huang, J. Li, H. Shao, J. Jiang, N. Chen, Ti₃C₂T_x/nonwoven fabric composite: promising MXene-coated fabric for wearable piezoresistive pressure sensors, *ACS Appl. Mater. Interfaces* 14 (2022) 9632–9643.
- Q. Zhang, R. Fan, W. Cheng, P. Ji, J. Sheng, Q. Liao, H. Lai, X. Fu, C. Zhang, H. Li, Synthesis of large-area MXenes with high yields through power-focused delamination utilizing vortex kinetic energy, *Adv. Sci.* (2022) 2202748.
- X. Ming, A. Guo, Q. Zhang, Z. Guo, F. Yu, B. Hou, Y. Wang, K.P. Homewood, X. Wang, 3D macroscopic graphene oxide/MXene architectures for multifunctional water purification, *Carbon* 16 (2020) 285–295.
- H. Lin, X. Wang, L. Yu, Y. Chen, J. Shi, H. Lin, L. Yu, Two-dimensional ultrathin MXene ceramic nanosheets for photothermal conversion, *Nano Lett.* 17 (2017) 384–391.

- [39] Y.-T. Liu, P. Zhang, N. Sun, B. Anasori, Q.-Z. Zhu, H. Liu, Y. Gogotsi, B. Xu, Self-assembly of transition metal oxide nanostructures on MXene nanosheets for fast and stable lithium storage, *Adv. Mater.* 30 (2018) 1707334.
- [40] L. Ding, Y. Wei, Y. Wang, H. Chen, H. Wang, J. Caro, A two-dimensional lamellar membrane: MXene nanosheet stacks, *Angew. Chem. Int. Ed.* 56 (2017) 1825–1829.
- [41] X. Wang, C. Garnero, G. Rochard, D. Magne, S. Morisset, S. Hurand, P. Chartier, J. Rousseau, T. Cabioch, C. Coutanceau, V. Mauchamp, S. Celerier, A new etching environment (FeF₃/HCl) for the synthesis of two-dimensional titanium carbide MXenes: a route towards selective reactivity vs. water, *J. Mater. Chem. A* 5 (2017) 22012–22023.
- [42] Q. Zhang, H. Lai, R. Fan, P. Ji, X. Fu, H. Li, High concentration of Ti₃C₂T_x MXene in organic solvent, *ACS Nano* 15 (2021) 5249–5262.
- [43] J. Yan, C.E. Ren, K. Maleski, C.B. Hatter, B. Anasori, P. Urbankowski, A. Sarycheva, Y. Gogotsi, Flexible MXene/Graphene films for ultrafast supercapacitors with outstanding volumetric capacitance, *Adv. Funct. Mater.* 27 (2017) 1701264.
- [44] X. Fan, Y. Ding, Y. Liu, J. Liang, Y. Chen, Plasmonic Ti₃C₂T_x MXene enables highly efficient photothermal conversion for healable and transparent wearable device, *ACS Nano* 13 (2019) 8124–8134.
- [45] R.P. Pandey, K. Rasool, E.M. Vinod, B. Aissa, Y. Gogotsi, K.A. Mahmoud, Ultrahigh-flux and fouling-resistant membrane based on layered silver/MXene(Ti₃C₂T_x) nanosheets, *J. Mater. Chem. A* 6 (2018) 3522–3533.
- [46] C.J. Zhang, S. Pinilla, N. McEvoy, C.P. Cullen, B. Anasori, E. Long, S.-H. Park, A. Seral-Ascaso, A. Shmeliov, D. Krishnan, C. Morant, X. Liu, G.S. Duesberg, Y. Gogotsi, V. Nicolosi, Oxidation stability of colloidal two-dimensional titanium carbides (MXenes), *Chem. Mater.* 29 (2017) 4848–4856.
- [47] J. Zhang, N. Kong, S. Uzun, A. Levitt, S. Seyedin, P.A. Lynch, S. Qin, M. Han, W. Yang, J. Liu, X. Wang, Y. Gogotsi, J.M. Razal, Scalable manufacturing of free-standing, strong Ti₃C₂T_x MXene films with outstanding conductivity, *Adv. Mater.* 32 (2020) 2001093.
- [48] X. Song, H. Wang, S. Jin, M. Lv, Y. Zhang, X. Kong, H. Xu, T. Ma, X. Luo, H. Tan, D. Hu, C. Deng, X. Chang, J. Xu, Oligolayered Ti₃C₂T_x MXene towards high performance lithium/sodium storage, *Nano Res.* 13 (2020) 1659–1667.
- [49] J. Halim, K.M. Cook, M. Naguib, P. Eklund, Y. Gogotsi, J. Rosen, M.W. Barsoum, X-ray photoelectron spectroscopy of select multi-layered transition metal carbides (MXenes), *Appl. Surf. Sci.* 362 (2016) 406–417.
- [50] O. Martin, A.J. Martin, C. Mondelli, S. Mitchell, T.F. Segawa, R. Hauert, C. Drouilly, D. Curulla-Ferre, J. Perez-Ramirez, Indium oxide as a superior catalyst for methanol synthesis by CO₂ hydrogenation, *Angew. Chem. Int. Ed.* 55 (2016) 6261–6265.
- [51] C. Ji, Y. Wang, Z. Ye, L. Tan, D. Mao, W. Zhao, X. Zeng, C. Yan, R. Sun, D.J. Kang, J. Xu, C.P. Wong, Ice-templated MXene/Ag-epoxy nanocomposites as high-performance thermal management materials, *ACS Appl. Mater. Interfaces* 12 (2020) 24298–24307.
- [52] K. Wang, H. Jiang, H. Liu, H. Chen, F. Zhang, Accelerated direct hydroxylation of aryl chlorides with water to phenols via the proximity effect in a heterogeneous metallaphotocatalyst, *ACS Catal.* 12 (2022) 6068–6080.